Safe and Energy-Efficient Jerk-Controlled Speed Profiling for On-Road Autonomous Vehicles

Fadel Tarhini, Reine Talj, Moustapha Doumiati

Safe and Energy-Efficient Jerk-Controlled Speed Profiling for On-road Autonomous Vehicles

Fadel Tarhini, Reine Talj, and Moustapha Doumiati

***Abstract*—Efficient speed planning is crucial for the safe and comfortable navigation of autonomous vehicles in dynamic environments. This paper introduces a novel energy-efficient, jerk-controlled speed planning approach based on quintic polynomial generation. We present a systematic methodology to determine the dynamic speed of autonomous vehicles by integrating several factors, including the relative velocity with dynamic obstacles, the curvature of the base frame and optimal selected path, road adherence, and road gradient. The direct integration of road adherence and gradient into the speed profiling approach contributes to improving vehicle safety. Comparative analysis with literature methods demonstrates the significant impact of jerk smoothness on energy efficiency. Simulations are conducted in a joint simulation between Simulink/Matlab and SCANeR Studio vehicle dynamics simulator, followed by validation on a real-world dataset. Our findings elucidate the significance of the proposed planning method in enhancing safety, energy economy, driving comfort, and computational efficiency, while effectively addressing a wide range of critical situations.**

***Index Terms*—Autonomous vehicles, motion planning, speed planning, safety, energy economy.**

I. Introduction

AUTOMATED driving heralds a reframing era in transportation with far-reaching implications for safety, efficiency, accessibility, and productivity. At its core, trajectory planning serves as the linchpin for enabling safe, efficient, and intelligent navigation within dynamic and stochastic environments [1]. This task entails the construction of comprehensive situational awareness, upon which complex decision-making processes operate to ascertain optimal trajectories while adhering to a spectrum of constraints [2], [3].

A trajectory planning problem involves identifying the most efficient path, complete with time-stamped positions, orientations, and velocities, from the vehicle's current state to a designated goal configuration. This optimization task aims to minimize specific objectives while adhering to various constraints, including geometric limitations (ensuring feasible paths within free space), task-specific constraints, and kinodynamic constraints. Such problems are recognized as PSPACE-hard, indicating that no polynomial-time algorithm exists to solve all instances of the problem [4]. In addition, finding an initial guess to solve the problem in the spatio-temporal space is non-trivial, sometimes even harder than solving the optimization problem [5]. Therefore, path-speed decoupled approaches partition the high-dimensional problem into two more manageable subproblems: initially, spatial path planning, followed by generating a speed profile along that path (temporal planning). This strategy facilitates a step-wise process, allowing for more efficient and tractable solutions to be obtained for each component independently.

Beyond learning-based methods, trajectory planning methodologies are generally classified into three main categories: sampling-based, search-based, and optimization-based methods. Sampling-based strategies may employ random techniques, such as Probabilistic Road Maps [6] and Rapidly-exploring Random Trees [7], or deterministic approaches, including control state and state space sampling methods [8]–[10]. For example, [11] proposes a sampling-based method that generates the coordinates (x, y) directly using fifth-degree polynomials of time. The generated paths resulting from random sampling methods often exhibit jerky motion, redundancy, and lack of curvature continuity, rendering them unsuitable for autonomous driving applications, particularly at high speeds. Additionally, the runtime of these methods is unbounded and unpredictable, further hindering their practical utility in real-time applications. Relative to random sampling-based techniques, deterministic sampling-based methods substantially diminish the solution space by exploiting the inherent structure of roadways. This deliberate reduction enhances predictability in planner behavior and mitigates the potential selection of impractical sampling seeds. However, the optimality of the selected path correlates directly with the longitudinal and lateral resolution of the generated path candidates. Enhancing path optimality entails reducing the resolution of generated paths, albeit at the cost of increased computational complexity. The search-based methods employ graph-based search techniques such as the fast search trees, A^* algorithm, along with state-lattice methods [12], [13]. In contrast to the random exploration of the environment's free space during run-time, search-based methods discretize the configuration space using a predefined set of motion primitives. These approaches proactively construct the search graph, facilitating a structured exploration of potential trajectories. Nevertheless, due to the discrete nature of the graph, inadequately designed search spaces can significantly reduce the solution space. This may result in highly sub-optimal solutions or even the absence of a solution, despite its existence. They demonstrate efficacy in low-speed unstructured environments [14]; however, the resulting paths often lack curvature continuity, rendering them unsuitable

This work is carried out within the framework of the V3EA project "Electric, Energy Efficient, and Autonomous Vehicle" (2021-2025), funded by the Research National Agency (ANR) of the French government.

Fadel Tarhini and Reine Talj are with Université de Technologie de Compiègne, CNRS, Heudiasyc UMR 7253, Compiègne, France (email: fadeltarhini@hds.utc.fr, reine.talj@hds.utc.fr).

Moustapha Doumiati is with ESEO-IREENA Lab UR 4642, Angers, France (email: moustapha.doumiati@eseo.fr).

for high-speed autonomous driving. While a post-smoothing process can render the generated path feasible for on-road driving scenarios, it compromises the collision-free property initially guaranteed by the search-based generation. Finally, optimization-based methods are variational methods that solve two-point boundary value problems utilizing nonlinear optimization methods. These methods excel in delivering optimal solutions characterized by embedded high-order curves or dense waypoint curves. However, in addition to computational complexity, they exhibit limitations in managing environmental complexity, as this complexity is dictated not solely by the number of obstacles but also by the geometric shape of the free space. Recently, seeking to solve this problem, numerous studies have considered integrating sampling methods with optimization methods [15]–[17]. Subsequent to path selection, a process of refinement is undertaken through nonlinear optimization, aimed at minimizing predefined cost functions.

Despite receiving less emphasis compared to spatial path planning, speed planning is increasingly recognized as an indispensable component in trajectory planning for autonomous vehicles. Responsible for generating optimal velocities along planned paths, speed planning is instrumental in ensuring critical aspects such as safety, comfort, energy efficiency, and traffic flow management. Speed planning methods existing in the literature can be categorized into four categories: search-based, optimization-based, learning-based, and switch-point methods (bang-bang). Methods in the literature tend to solve the minimum-time problem [18] by employing these techniques. In the context of the search-based methods, [19] employs a visibility graph with dynamic obstacles, speed, and acceleration constraints. An inherent limitation of these methods lies in their incapacity to directly maximize smoothness. Consequently, the speed profiles derived necessitate supplementary smoothing to ensure optimal driving comfort. This smoothing process can pose challenges, particularly in scenarios where the solution obtained from the search-based method approaches constraint limits. In such cases, the smoothing procedure itself becomes a constrained optimization problem, adding complexity to the solution process. Contrary to search-based methods, optimization-based methods [20], [21] can maximize smoothness directly. However, these methods encounter challenges in handling dynamic obstacles due to their non-convex nature in the $(s-t)$ domain [22]. The majority of literature either neglects the inclusion of dynamic obstacles in their optimization framework or restricts the problem to solvable scenarios [23]. A novel approach presented by [24] addresses this limitation by introducing a new formulation that accounts for dynamic obstacles, with the problem iteratively solved as a quadratic program. However, the proposed method is computationally expensive. Switch-point methods [25] demonstrate that for the time-optimal problem, the optimal solution invariably involves either maximum acceleration or deceleration. Consequently, the challenge becomes identifying the switch-points to alternate between these two extremes. Finally, learning-based methods can be employed for speed planning [26]. For instance, [27] employs reinforcement learning to generate an efficient speed profile by minimizing the battery state-of-charge (SOC). However, these methods suffer from sample inefficiency, often demanding extensive data collection for effective learning. In addition, generalization remains an issue, with learned policies struggling to adapt to diverse real-world scenarios.

Energy efficiency is emerging as a primary concern in spatial path planning [28], behavioral planning [29], and speed planning [30]. Existing methods for energy economic speed planning involve the minimization of the battery SOC through either learning-based methods [31] or optimization [32]. In this work, we present a novel methodology for energy-efficient speed planning. As stated in [33] and in our previous work [34], the smoothness of the velocity profile and the fluctuations in the acceleration profile directly impact the energy efficiency of the autonomous vehicle. Alternatively, the primary contributors to uncomfortable driving are elevated levels of jerk and acceleration, with jerk exerting a more pronounced influence than acceleration [35]. Consequently, various studies have introduced jerk-limited speed planning techniques [36], [37] aimed at enhancing the similarity between automated and human-like driving. In this paper, we introduce a quintic jerk-controlled speed planning approach. Leveraging the cubic jerk profile to achieve a smooth curve with second-order continuity, our method emphasizes an energy-efficient trajectory.

Literature shows that the majority of motion planning techniques emphasize path and speed optimization, often relying on computationally demanding approaches without adequately considering the trade-off between optimality and computational efficiency. Research studies often overlook the comprehensive examination of the global system architecture and the inherent delays among its constituent elements, including sensor acquisition, perception, decision-making, planning, control, and actuators. Particularly for on-road autonomous vehicles operating at medium-to-high speeds, deterministic behavior is essential at higher sampling rates. Therefore, it demonstrates the necessity for a rapid and energy-efficient speed planning method that accounts for the dynamic environment, driving comfort, and safety.

In this work, we introduce a novel rapid energy-efficient jerk-controlled fifth-order speed planning method that accounts for road geometry and conditions, and dynamic obstacles. The simulations are conducted using: 1) a joint-simulation framework with the professional SCANeR Studio vehicle dynamics simulator, utilizing a fully dynamic vehicle model, and 2) a real-world dataset using a full nonlinear vehicle model [34]. This approach contrasts with many existing literature studies, which often rely on simpler vehicle models. By employing a comprehensive vehicle dynamics model, our simulations provide a more realistic representation of real-world driving scenarios. The conducted scenarios encompass roads featuring high-curvature corners, with certain situations of overtaking dynamic obstacles and avoiding static obstacles. Other scenarios are performed on adherence-changing and gradient-variant roads to target and highlight our contributions. By incorporating considerations for the relative velocity of dynamic obstacles and the curvature of the selected best path, our method demonstrates efficient speed planning during lane-changing maneuvers on structured roads.

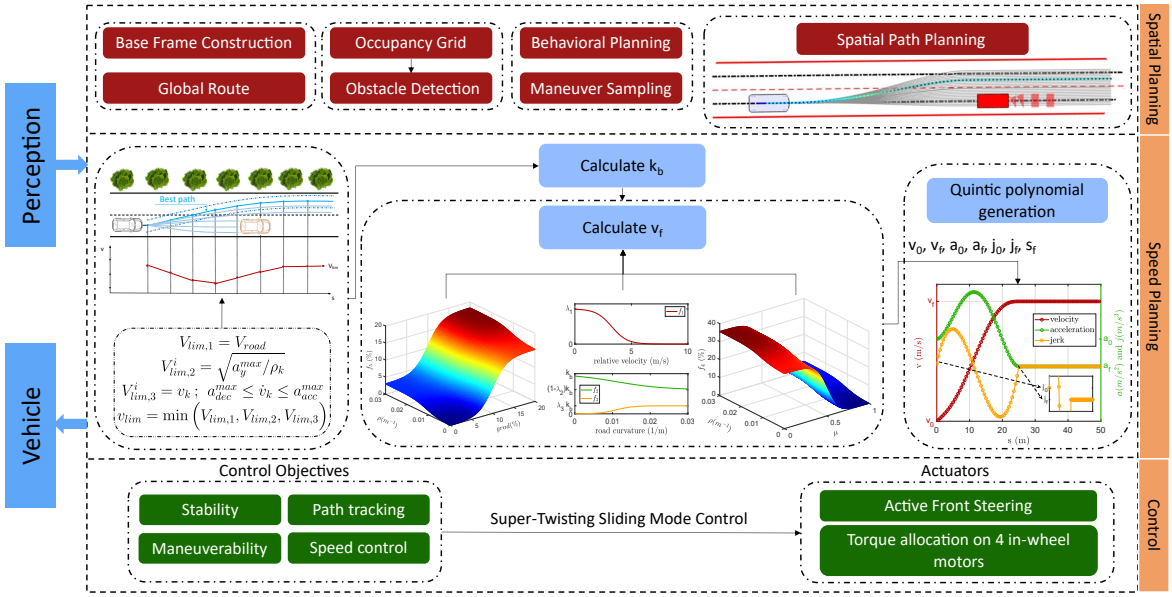

Fig. 1: Schematic diagram of the proposed global system architecture.

The contributions of the paper can be outlined as:

- Development of a jerk-controlled speed planning method based on a novel formulation of fifth-order polynomial generation, comprising transient and steady phases.
- Introducing a planning parameter that incorporates the relative velocity between the vehicle and dynamic obstacles, the curvature of the base frame, the curvature of the best path, and road conditions.
- Novel consideration of road adherence and gradient directly integrated into the speed planning approach, significantly enhancing vehicle safety and energy efficiency.
- Illustrating the impact of jerk smoothness on the energy efficiency of speed planning through a comparative analysis between the quintic polynomial and cubic one.

The rest of the paper is organized as follows: Section II introduces the complete system architecture. Section III presents the spatial planning method. Section IV develops the speed planning approach. The system validation is presented in Section V followed by a conclusion in Section VI.

II. System Architecture

The global system architecture is given in Fig. 1. The output of the perception module is received as an occupancy grid representation. Detailed discussion of this module is beyond the scope of the paper. During each planning iteration, the local occupancy grid undergoes updates to accommodate the new footprint occupied by moving obstacles within its perception zone. The longitudinal expansion of the occupancy of the moving obstacles is adjusted to reflect their velocity and direction, based on the predicted traveled distance, and updated each iteration. Then, the spatial path planning module, detailed in Section III, executes a sampling-based path generation process. For each point on the navigable candidate paths, the footprint of the vehicle is validated according to the method of six circles and one large circle [4]. The six circles are only examined when an obstacle is detected. Consequently, for an obstacle-free path, a single large circle is inspected, as opposed to the four-circle approach [14], providing enhanced computational efficiency. The local occupancy grid is then transformed into a clearance map to improve accuracy and efficiency. Subsequent to the selection of the best path, a novel speed-planning method, detailed in Section IV, is proceeded on the selected path. The approach commences by establishing the velocity limit at each knot of the chosen path. Subsequently, a parameter k_b is derived from these limits. Then, a planning parameter v_f is ascertained, integrating k_b, the relative velocity with obstacles, the curvature of both the base frame and the optimal path, and road adherence and gradient. Finally, a quintic energy-efficient polynomial is generated for the speed along the path. Finally, the control layer comprises the achievement of several objectives including stability, maneuverability, path-tracking, and speed control, leveraging the Super-Twisting Sliding Mode control. Then, the control inputs are realized by physical actuators including four in-wheel motors. The reader can refer to the authors' previous works on this level [38], [39]. Ultimately, the steering angle and the generated torques are fed into a full nonlinear vehicle model developed by [40], and then validated on the SCANeR Studio professional vehicle dynamics simulator [41].

III. Spatial Path Planning

To mimic human drivers' behavior in structured environments, it is practical for the trajectory planner to generate road geometry-aligned paths, where the solution space is significantly reduced. In this paper, we employ a sampling-based method in which the generated paths traverse a transition state and a steady state in parallel to each other, similar to [9], [10]. The planning method is executed in 3 stages, with base frame construction at the first stage. Then, the path generation is executed in the Frenet system (s, q), where the paths are shifted by a lateral offset from the base frame. Finally, the best path with the lowest introduced cost is selected.

A. Base Frame Construction

The base frame represents a global route used to provide reference road information. It constitutes a sequence of waypoints and is modeled by a parametric curve. The cubic spline is adopted in this work which is sufficiently expressive to satisfy positional constraints, tangency conditions, and curvature constraints, all while preserving a desirable low order in parametrization. Denoting s as the arc length of every segment, and i as the waypoint index, the cubic spline is expressed as

$$\begin{cases} x_{bf}(s) = a_0 + a_1(s-s_i) + a_2(s-s_i)^2 + a_3(s-s_i)^3 \\ y_{bf}(s) = b_0 + b_1(s-s_i) + b_2(s-s_i)^2 + b_3(s-s_i)^3 \end{cases} \tag{1}$$

where (x_{bf}, y_{bf}) are the Cartesian coordinates of the point on the base frame, and $\{(a_j, b_j), j = 0,1,2,3\}$ are the fitting parameters. The heading θ_{bf} and curvature ρ_{bf} of every point of the base frame can be determined by

$$\theta_{bf} = \frac{dy_{bf}}{dx_{bf}}; \quad \rho_{bf} = \frac{x'_{bf}y''_{bf} - x''_{bf}y'_{bf}}{\sqrt{(x'_{bf} + y'_{bf})^3}} \tag{2}$$

where $x'_{bf}, y'_{bf}, x''_{bf}, y''_{bf}$ are the first and second derivatives of x_{bf} and y_{bf}.

B. Path Candidates Generation

The objective of the path planning strategy is to identify the optimal path from a set of generated candidates, excluding those deemed non-navigable. Non-navigable paths are defined as those intersecting static and dynamic obstacles within an adapted security distance [10], or failing to adhere to established safety criteria. Hence, the navigation strategy comprises several stages: generation of candidate paths, obstacle detection, path classification, and path selection (see Fig. 2).

The initial phase entails localizing the vehicle within the base frame. This process involves mapping the vehicle's Cartesian coordinates to the $(s-q)$ coordinate system and subsequently determining the closest point on the base frame utilizing a combination of quadratic minimization and Newton's method [10]. From the matched point $P_i(s_i, \rho_i)$, the path candidates are generated in two phases: transition phase ($s \in [s_i, s_{f0}]$) and a steady phase ($s \in [s_{f0}, s_f]$) (see Fig. 3). The length of the phases is proportional to the speed of the vehicle v and bounded between a minimum Δs_{min} and a maximum Δs_{max}.

$$\begin{aligned} s_{f0} &= \Delta s_{min} + k_v v \\ s_f &= \min(\Delta s_{max}, s_{f0} + 2d_{ss}) \end{aligned} \tag{3}$$

where k_v is a gain parameter and d_{ss} is the safe stop distance given by (4).

$$d_{ss} = d_{ss,0} + \frac{v^2}{2a_{dec}^{max}} \tag{4}$$

where a_{dec}^{max} is the maximum acceptable longitudinal deceleration and $d_{ss,0}$ is the minimum safety gap.

$$q(s) = \begin{cases} c_0 + c_1(s-s_i) + c_2(s-s_i)^2 \\ \quad + c_3(s-s_i)^3 + c_4(s-s_i)^4 & s \in [s_i, s_{f0}] \\ q_{f,j} & s \in [s_{f0}, s_f] \end{cases} \tag{5}$$

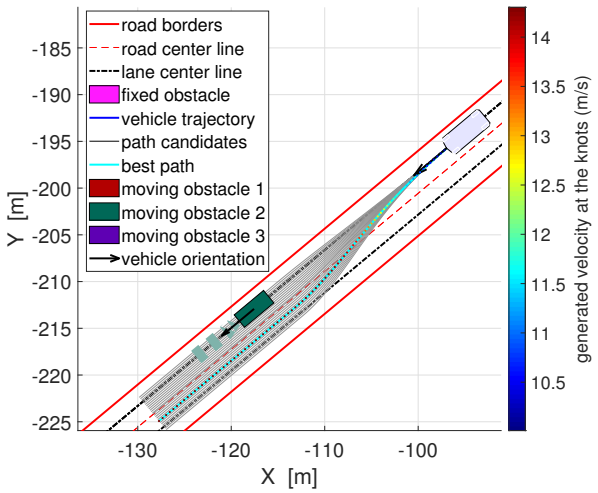

Fig. 2: Proposed trajectory planning method for an overtaking scenario involving a dynamic obstacle. The legend is shared with Figures 9, 14 and 18. Legend components not shown in this Figure are depicted in other figures. Rectangular hatches indicate the longitudinal expansion of the dynamic obstacle. The colormap represents the quintic speed profile generation along the knots constituting the best path.

Note that adding $2d_{ss}$ to (3) serves to include safety margins alongside comfortable deceleration. To ensure the $\mathscr{L}^2$ continuity and avoid curvature discontinuity, a fourth-order polynomial is generated representing the path candidates (5). The coefficients c_i of each path candidate j can be determined by solving the following boundary conditions problem

$$\begin{aligned} &q(s_i) = q_i\ , \quad \rho(s_i) = \rho_i\ , \quad q(s_{f0}) = q_{f,j} \\ &\frac{\partial q}{\partial s}|_{s_i} = \tan\Delta\theta_i\ , \quad \frac{\partial q}{\partial s}|_{s_{f0}} = 0 \end{aligned} \tag{6}$$

where $\Delta\theta_i$ is the difference between the vehicle heading angle and the tangent at $P_i(s_i, \rho_i)$. For each path candidate j, there exists a corresponding lateral offset $q_{f,j}$. These lateral offsets are spaced apart by a constant lateral resolution Δq, with the total number of offsets determined by the lane boundaries. The lane boundaries are determined by subtracting the vehicle width from the lane width to prevent candidate paths from being generated near the lane borders. Path candidates comprises a set of n points (knots) dispersed with a constant longitudinal resolution Δs. Their number vary depending on the arc length of the path candidates s_f (see Fig. 3). Path candidates generated in the $(s-q)$ coordinate system are mapped into the Cartesian system to conform to the maneuvering system. The corresponding points in the Cartesian system can be represented in terms of the arc length of the base frame [42] as

$$\frac{\partial x}{\partial s} = Q\cos\theta\ , \quad \frac{\partial y}{\partial s} = Q\sin\theta\ , \quad \frac{\partial \theta}{\partial s} = Q\rho \tag{7}$$

where ρ, the curvature of the path candidates, can be calculated as

$$\rho = \frac{S}{Q}\left(\rho_{bf} + \frac{(1-q\rho_{bf})(\frac{\partial^2 q}{\partial s^2}) + \rho_{bf}(\frac{\partial q}{\partial s})^2}{Q^2}\right) \tag{8}$$

where,

$$Q = \sqrt{(\frac{\partial q}{\partial s})^2 + (1-q\rho_{bf})^2}\ , \quad S = sgn(1-q\rho_{bf}) \tag{9}$$

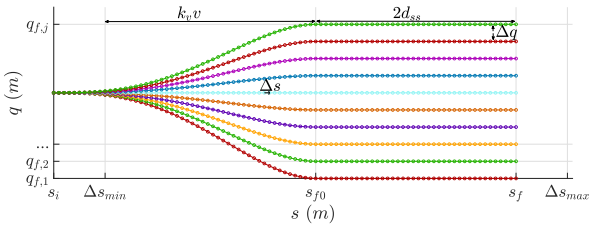

Fig. 3: Generation of the path candidates with lateral resolution Δq and longitudinal resolution Δs in the (s, q) frame. Δs_{min} represents the minimum threshold for s_{f0}, while Δs_{max} serves as the maximum limit for s_f, chosen based on kinodynamic constraints and the vehicle's perception zone.

Upon the generation of the set of path candidates, those intersecting with detected obstacles within the security distance are discarded, along with paths that do not adhere to the kinodynamic constraints.

C. Path Selection

The path selection process is conducted to determine the optimal path from the set of navigable paths, minimizing a cost function that incorporates various criteria (see Fig. 2). Given that the curve with the highest smoothness is the curve of least energy, we integrate J_1 as the energy cost. J_2, denoting the consistency cost, can also be interpreted as an energy cost, as abrupt changes in trajectory demand additional energy and higher control effort. Further, to force the vehicle to maintain proximity to the reference lane, a reference offset cost term J_3 is introduced. Hence, for each path i from the set of navigable paths, J_1, J_2, J_3 are given as

$$J_1[i] = \int \rho_i^2 \, ds \tag{10a}$$

$$J_2[i] = i^*|_t - i^*|_{t-1} \tag{10b}$$

$$J_3[i] = \int (q_i - q_{ref})^2 \, ds \tag{10c}$$

where i^* is the path index and q_{ref} is the lateral offset of the reference lane from the base frame. The final cost term J_4 is a safety term consisting of longitudinal safety cost $J_{4,1}$ (pertaining host lane navigability) and a lateral safety cost $J_{4,2}$ (concerning adjacent lane navigability) [10].

$$J_{4,1}[i] = 2 - \frac{2}{1 + e^{-(c_s \, d_{obs}[i])}} \tag{11a}$$

$$g[k] = \frac{1}{\sqrt{2\pi}\sigma} e^{-\frac{(k\Delta q)^2}{2\sigma^2}} \tag{11b}$$

$$J_{4,2}[i] = \frac{\sum_{k \in \Gamma_i} J_{4,1}[k] g[i-k]}{N} \tag{11c}$$

$$J_4[i] = J_{4,1} + w_s J_{4,2} \tag{11d}$$

where c_s is a tunable parameter and $d_{obs}[i]$ is the distance-to-obstacle (collision distance) on the path i. $g[k]$ is the discrete inverted Gaussian convolution, σ is the standard deviation of collision risk, and Δq is the lateral sampling resolution. Γ_i is the set of navigable paths excluding the path i, N is their number, and w_s is a weighting coefficient. The designed costs are normalized using (12a), and the total cost is given by (12b)

$$\overline{J}_r[i] = \frac{J_r[i] - \min\left(J_r[i]\right)}{\max\left(J_r[i]\right) - \min\left(J_r[i]\right)}; \; r = \{1, 2, 3, 4\} \tag{12a}$$

$$J_T[i] = w_1 \overline{J_1}[i] + w_2 \overline{J_2}[i] + w_3 \overline{J_3}[i] + w_4 \overline{J_4}[i] \tag{12b}$$

Algorithm 1 Acceleration limitation for $V_{lim,3}$

```
for each knot k do
    if v_{k+1} > v_k then
        if v_{k+1}^2 - v_k^2 > 2Δs a_acc^com then
            v_{k+1} = sqrt(v_k^2 + 2Δs a_acc^com)
        end if
    else
        if v_k^2 - v_{k+1}^2 > 2Δs |a_dec^com| then
            v_k = sqrt(v_{k+1}^2 + 2Δs |a_dec^com|)
        end if
    end if
end for
```

where w_1, w_2, w_3, w_4 are the weighting coefficients for energy, consistency, reference, and safety cost terms respectively.

IV. Speed Planning

A speed profile is generated along the selected best path to incorporate temporal information into trajectory planning. This profile is designed to adhere to the traffic rules and road code, account for static and dynamic obstacles, and adjust according to prevailing road conditions. Hence, this section focuses on an energy-efficient quintic polynomial generation for speed planning, accounting for velocity limitation, obstacles, curvature of the base frame and best path, road adherence, and road gradient (slope).

A. Velocity Limitation

Velocity limitations are imposed on the autonomous vehicle to ensure compliance with on-road regulations and enhance driving comfort. The first limitation $V_{lim,1}$ (13a) concerns traffic rules (traffic lights and road signs), and is presumed to be known to the vehicle. The second limitation $V_{lim,2}$ (13b) is enforced to enhance comfort by keeping the lateral acceleration a_y below a threshold $a_y^{max} = 4\ m/s^2$. The limit is calculated at every knot k of the candidate paths, knowing the curvature at each point ρ_k (8). After the construction of the velocity limits at each knot along the path candidates, $V_{lim,3}$ (13c) is applied to guarantee that the speed transition between two consecutive knots does not exceed the maximum comfortable acceleration/deceleration threshold.

$$V_{lim,1} = V_{road} \tag{13a}$$

$$V_{lim,2} = \sqrt{a_y^{max}/\rho_k} \tag{13b}$$

$$V_{lim,3} = v_k \; ; \;\; a_{dec}^{com} \leq \dot{v}_k \leq a_{acc}^{com} \tag{13c}$$

$$v_{lim} = \min\left(V_{lim,1}, V_{lim,2}, V_{lim,3}\right) \tag{13d}$$

Hence, to confine the transition within the limits of a maximum comfortable deceleration threshold a_{dec}^{com} and a maximum comfortable acceleration threshold a_{acc}^{com}, Algorithm 1 is employed. The algorithm acts to saturate the velocity at the knot $k{+}1$ if the velocity rate of change between k and $k{+}1$ exceeds the acceleration limits. Finally, the velocity limitation along the paths is given by the minimum of the three limitations (13d).

B. Quintic polynomial generation

The speed profile along the best path is generated based on a novel formulation of quintic polynomials, comprising transient and steady phases. This approach aims to achieve a smooth third-order profile for the jerk with $\mathscr{C}^2$ continuity. It will be demonstrated that the smoothness of the jerk profile directly contributes to improved energy efficiency.

A quintic polynomial for velocity $v(t)$ is given as

$$v(t) = \sum_{i=0}^{5} \xi_i t^i \tag{14}$$

where ξ_i, $\{i = 0, 1, 2, ..., 5\}$ are the polynomial coefficients. To calculate ξ_i, a total of seven boundary conditions are required, as the traveling time along the path (t_f) is unknown. Hence we have,

$$v(0) = \xi_0 = v_0 \tag{15a}$$
$$v(t_f) = v_0 + \xi_1 t_f + \xi_2 t_f^2 + \xi_3 t_f^3 + \xi_4 t_f^4 + \xi_5 t_f^5 = v_f \tag{15b}$$
$$a(0) = \xi_1 = a_0 \tag{15c}$$
$$a(t_f) = \xi_1 + 2\xi_2 t_f + 3\xi_3 t_f^2 + 4\xi_4 t_f^3 + 5\xi_5 t_f^4 = a_f \tag{15d}$$
$$j(0) = 2\xi_2 = j_0 \tag{15e}$$
$$j(t_f) = 2\xi_2 + 6\xi_3 t_f + 12\xi_4 t_f^2 + 20\xi_5 t_f^3 = j_f \tag{15f}$$
$$s(t_f) = v_0 t_f + \frac{1}{2}\xi_1 t_f^2 + \frac{1}{3}\xi_2 t_f^3 + \frac{1}{4}\xi_3 t_f^4 + \frac{1}{5}\xi_4 t_f^5 + \frac{1}{6}\xi_5 t_f^6 = s_f \tag{15g}$$

where v_0, a_0, j_0 and v_f, a_f, j_f are the velocity, acceleration, and jerk at the initial and the final points of the polynomial. s_f represents the length of the best path and t_f is the traveling time along it. Hence, given $\{v_0, v_f, a_0, a_f, j_0, j_f, s_f\}$, we solve for $\{\xi_0, \xi_1, \xi_2, \xi_3, \xi_4, \xi_5, t_f\}$ using (15). The calculation of the first three coefficients is trivial and can be solved as

$$\xi_0 = v_0 \; ; \quad \xi_1 = a_0 \; ; \quad \xi_2 = \frac{j_0}{2} \tag{16}$$

To determine the remnant coefficients and by manipulating the equations of (15), one has to calculate t_f first by solving the cubic equation (17).

$$\alpha_3 t_f^3 + \alpha_2 t_f^2 + \alpha_1 t_f + \alpha_0 = 0 \tag{17a}$$
$$\alpha_3 = \frac{-1}{120} j_0 + \frac{-1}{120} j_f \tag{17b}$$
$$\alpha_2 = \frac{-1}{10} a_0 + \frac{1}{5} a_f \tag{17c}$$
$$\alpha_1 = \frac{-1}{2} v_0 + \frac{-1}{2} v_f \tag{17d}$$
$$\alpha_0 = s_f \tag{17e}$$

where α_i are the coefficients of the cubic equation. Finally, ξ_5, ξ_4, and ξ_3 can be calculated iteratively as (18).

$$\xi_5 = \frac{-3}{10}\Big[\frac{(\frac{7}{3} j_0 - j_f) t_f^3 + (18 a_0 - 2 a_f) t_f^2 + (60 v_0 + 20 v_f) t_f}{t_f^6} \frac{-80 s_f}{t_f^6}\Big] \tag{18a}$$

$$\xi_4 = \frac{-10\xi_5 t_f^4 + j_f t_f + j_0 t_f - 2a_f + 2a_0}{4 t_f^3} \tag{18b}$$

$$\xi_3 = \frac{-20\xi_5 t_f^3 - 12\xi_4 t_f^2 + j_f - j_0}{6 t_f} \tag{18c}$$

Given that the path having n knots, the quintic polynomial is sampled on $n - p$ knots and becomes steady on the remnant p knots ($v|_n = v|_{n-1} = ... = v|_{n-p}$). The initial and final boundary conditions are updated at each sampling iteration t_i as $v_0 = v(t_i)$, $a_0 = \frac{\partial v}{\partial t}|_{t_i}$, $j_0 = \frac{\partial^2 v}{\partial t^2}|_{t_i}$, and $a_f = j_f = 0$ (see the quintic polynomial generation in Fig. 1). Ultimately, the generation of the quintic polynomial hinges upon the core planning parameter v_f.

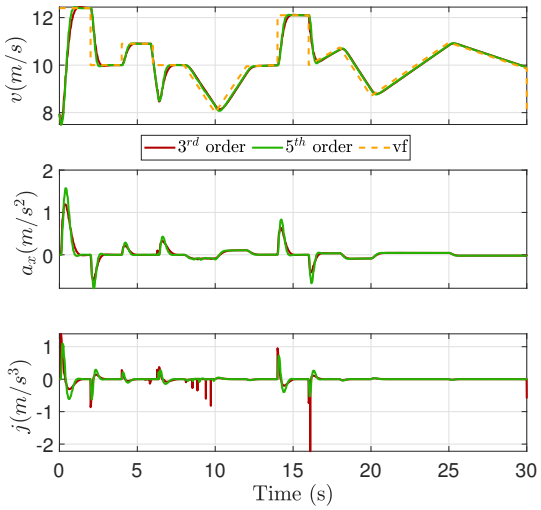

Fig. 4: Quintic and cubic speed profiling for an arbitrary v_f.

C. Cubic Polynomial Generation

To illustrate the direct correlation between energy efficiency and jerk smoothness, the quintic polynomial is contrasted with a cubic polynomial. We retain the ability to generate a cubic polynomial by enforcing $\xi_4 = \xi_5 = 0$. Hence, the cubic polynomial $v(t)$ is given as

$$v(t) = \sum_{i=0}^{3} \xi_i t^i \tag{19}$$

where $\xi_0, \xi_1, \xi_2, \xi_3$ are the polynomial coefficients. Following the same approach as in (15) without the boundaries on j (without the boundaries (15e) and (15f)), t_f can be calculated by solving the quadratic equation below.

$$\alpha_2 t_f^2 + \alpha_1 t_f + \alpha_0 = 0 \tag{20a}$$
$$\alpha_2 = a_0 - a_f \tag{20b}$$
$$\alpha_1 = 6 v_0 + 6 v_f \tag{20c}$$
$$\alpha_0 = -12 s_f \tag{20d}$$

where α_i are the coefficients of the quadratic equation. Subsequently, ξ_0, ξ_1, ξ_2 and ξ_3 are given by (21).

$$\xi_0 = v_0; \quad \xi_1 = a_0 \tag{21a}$$
$$\xi_2 = \frac{(-a_f - 2a_0) t_f - 3(v_0 - v_f)}{t_f^2} \tag{21b}$$
$$\xi_3 = \frac{(a_0 + a_f) t_f + 2(v_0 - v_f)}{t_f^3} \tag{21c}$$

Similar to the quintic polynomial, the cubic speed profiling is sampled along $n - p$ knots. Fig. 4 depicts the difference in speed profiling between the quintic and cubic polynomials for an arbitrary v_f. It is evident that while there may not be significant disparities in speed profile generation, the quintic

surpasses the cubic polynomial in terms of jerk. The jerk exhibited by the cubic polynomial is linear with oscillations and higher overshoots compared to the quintic polynomial which exhibits a smooth third-order jerk profile. The acceleration-optimal cubic profile exhibits lower acceleration values yet higher jerk values compared to the jerk-optimal quintic profile.

D. planning parameter v_f

The planning parameter v_f is the desired velocity at the $n-p$ knot of the selected best path, upon which the polynomial generation is based. This parameter is composed of several sub-functions, each addressing different aspects of road conditions and the dynamic environment. The novel formulation of the functions is conceived based upon: 1) capturing intricate nonlinearities, 2) providing smooth transitions with a capability of behavior adjustment, 3) ensuring continuity and differentiability, and 4) imposing constraints on boundedness and saturation to confine the outputs within a set of limits. The form of the functions will demonstrate exceptional effectiveness in achieving smoothness in the speed profile, concurrently addressing several objectives.

1) Relative velocity and curvature

When overtaking a dynamic obstacle in urban environments, it is crucial to accelerate (accounting to the relative velocity) to reduce exposure to oncoming traffic and ensure smooth traffic flow on the road. The acceleration reaches its maximum peak when the relative velocity is zero and decreases as the relative velocity increases (see Fig. 5 left). Given that the velocity of the surrounding dynamic obstacles is presumed to be known to the vehicle, let $v_r = \{v_{r,i} = v_{veh} - v_{obs,i}\ ;\ \ i = 1, 2, ..., n\}$ denote the relative velocity between the vehicle and the n surrounding obstacles within the perception zone. Hence, define the first sub-function f_1 as a function of relative velocity v_r as

$$f_1(v_r) = \lambda_1 \Big[1 - \frac{1}{1 + e^{-\frac{2\gamma_1}{\overline{v_r} - \underline{v_r}}(|v_r| - \frac{\overline{v_r} + \underline{v_r}}{2})}}\Big] \tag{22}$$

where λ_1 is a gain to specify the upper bound, γ_1 denotes the gradient intensity of the transient-state centroid, and $\underline{v_r}$, $\overline{v_r}$ signify the endpoints of the transient state of f_1. The aim of formulating f_1 is to provide the vehicle with additional acceleration when overtaking a dynamic obstacle.

The speed profile is anticipated to decrease with increasing road curvature. However, its rate of change with respect to the base frame curvature (global route) should vary from that of the best path (for instance during lane changes). Hence, define two sub-functions f_2 and f_3 function of curvature of the base frame (ρ_{bf}) and curvature of the best path (ρ_{bp}) as (23)

$$f_2(\rho_{bf}) = \Big[1 - \frac{\lambda_2}{1 + e^{-\frac{2\gamma_2}{\overline{\rho} - \underline{\rho}}(|\rho_{bf}| - \frac{\overline{\rho} + \underline{\rho}}{2})}}\Big] k_b \tag{23a}$$

$$f_3(\rho_{bf}, \rho_{bp}) = \frac{\lambda_3}{1 + e^{-\frac{2\gamma_3}{\overline{\rho} - \underline{\rho}}(|\rho_{bp} - \rho_{bf}| - \frac{\overline{\rho} + \underline{\rho}}{2})}} k_b \tag{23b}$$

where λ_2 and λ_3 provide a lower bound for f_2 and an upper bound for f_3 respectively, and k_b represents the base velocity. $\underline{\rho}$, $\overline{\rho}$ are the extremities of the transient state of f_2 and f_3, and γ_2, γ_3 are as γ_1. The form of the functions f_1, f_2, and f_3 is depicted in Fig. 5. Hence, starting from a base velocity k_b designated for zero curvature in both the base frame and the best path, f_2 and f_3 serve to progressively reduce the vehicle speed in response to increasing curvature.

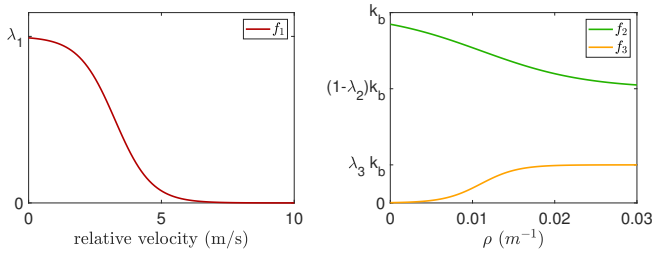

Fig. 5: Planning parameter v_f sub-functions: f_1, f_2 and f_3.

Therefore, define v_{f1} in terms of f_1, f_2, and f_3 as

$$v_{f1} = (k_t \times k_r \times k_s) \times f_1 + f_2 - f_3 \tag{24}$$

where k_t, k_r, and k_s are boolean functions. k_t, k_r, and k_s respectively act to activate f_1 according to the obstacle type, relative direction with the obstacle, and overtaking behavioral decision. $k_t = 1$ if the obstacle type is moving, and 0 otherwise. $k_r = 0$ if $sgn(v_{veh} v_{obs}) < 0$ (the vehicle and the obstacle are in opposite directions) and 1 otherwise. $k_s = 1$ if a behavioral decision is taken of overtaking the succeeding vehicle, and 0 otherwise. Hence, the boolean functions are set to promote f_1 only when overtaking a dynamic obstacle.

In some unpredictable situations, the value of v_f might exceed the velocity limitations (13) if k_b is not carefully set. Under such conditions, the reference profile will alternate as the minimum between the quintic generated profile and the velocity limitations at the knots, thereby leading to an oscillatory reference speed profile. This phenomenon induces fluctuations in acceleration and deceleration, consequently elevating energy consumption. Alternately, although setting k_b as a constant value below the minimum velocity limitation of the road can avert this oscillation, it tends to render the speed profile more conservative. Therefore, k_b is formulated according to the velocity limitation v_{lim} (13d) and the sampling time t_s as follows

$$k_b^i = \Big[\frac{v_{lim}^i - k_b^{i-1}}{t_s}\Big] \lambda_g + k_b^{i-1} \tag{25}$$

where λ_g is a tunable parameter. Thus, by varying k_b based on v_{lim}, the approach of selecting the minimum between v_{lim} and the quintic speed profile generated based on v_f can be relaxed if the difference between them is less than 2 m/s.

$$\Big| -\frac{2\gamma_1}{\overline{v_r} - \underline{v_r}} \lambda_1 \frac{\partial v_r}{\partial t} \frac{e^{-\frac{2\gamma_1}{\overline{v_r} - \underline{v_r}}(v_r - \frac{\overline{v_r} + \underline{v_r}}{2})}}{\Big(1 + e^{-\frac{2\gamma_1}{\overline{v_r} - \underline{v_r}}(v_r - \frac{\overline{v_r} + \underline{v_r}}{2})}\Big)^2} \Big| \leq |a_{dec}^{com}| \tag{26a}$$

$$\Big| -\frac{2\gamma_2}{\overline{\rho} - \underline{\rho}} k_b \lambda_2 \frac{\partial \rho_{bf}}{\partial t} \frac{e^{-\frac{2\gamma_2}{\overline{\rho} - \underline{\rho}}(\rho_{bf} - \frac{\overline{\rho} + \underline{\rho}}{2})}}{\Big(1 + e^{-\frac{2\gamma_2}{\overline{\rho} - \underline{\rho}}(\rho_{bf} - \frac{\overline{\rho} + \underline{\rho}}{2})}\Big)^2} \Big| \leq |a_{dec}^{com}| \tag{26b}$$

$$\Big| \frac{2\gamma_3}{\overline{\rho} - \underline{\rho}} k_b \lambda_3 \frac{\partial \rho_{bp}}{\partial t} \frac{e^{-\frac{2\gamma_3}{\overline{\rho} - \underline{\rho}}(\rho_{bp} - \frac{\overline{\rho} + \underline{\rho}}{2})}}{\Big(1 + e^{-\frac{2\gamma_2}{\overline{\rho} - \underline{\rho}}(\rho_{bp} - \frac{\overline{\rho} + \underline{\rho}}{2})}\Big)^2} \Big| \leq a_{acc}^{com} \tag{26c}$$

As f_2 and f_3 consistently vary with the continuous curvature, it is imperative to constrain their rate of change to time (representing acceleration), within the maximum admissible acceleration/deceleration. Similarly for f_1 with the variation of

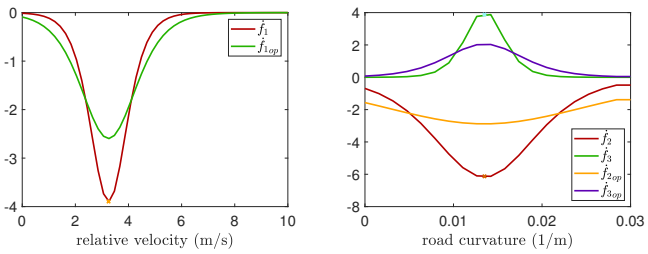

Fig. 6: Effect of optimizing γ_i on acceleration extremums.

the relative velocity. Hence the constraints on the formulation of the functions are given in (26). Given that the extremum of $\frac{\partial f_i}{\partial t}$ where $i = \{1, 2, 3\}$ is at the centroid of the transient state, it is sufficient to bound $\dot{f}_1$, $\dot{f}_2$, and $\dot{f}_3$ at $v_r = \frac{\overline{v_r}+\underline{v_r}}{2}$ and $\rho = \frac{\overline{\rho}+\underline{\rho}}{2}$ respectively. Hence, in a context of function shaping, an optimization problem is formulated to determine $\{\gamma_1, \gamma_2, \gamma_3\}$ such that

$$\begin{aligned} &\min\{\gamma_1, \gamma_2, \gamma_3\} \\ &\text{satisfying } \ (26a), (26b), (26c) \end{aligned} \tag{27}$$

Hence, by choosing the design parameters as $\overline{\rho} = 0.02, \underline{\rho} = 0.002, \overline{v_r} = 6, \underline{v_r} = 0.5, \lambda_1 = 3.5, \lambda_2 = 0.4$, and $\lambda_3 = 0.2$, the bounds of slope intensities are determined as $\gamma_1 \leq 4.6196$, $\gamma_2 \leq 1.4375$, and $\gamma_3 \leq 4.7917$. Fig. 6 illustrates the impact of optimizing γ_i in constraining the extremities of acceleration, wherein the optimal functions $\dot{f}_{op}$ are bounded below $a_{acc}^{com} = 2\ m/s^2$ and above $a_{dec}^{com} = -2.5\ m/s^2$. Hence, the longitudinal acceleration $a_x \in [-2.5\ \ 2]\ m/s^2$. Lateral acceleration is bounded by $a_y \in [-4\ \ 4]\ m/s^2$, and jerk is limited in $j \in [-3\ \ 3]\ m/s^3$. Velocity constraints are determined by v_{lim} (13d), while the quintic speed profile relies on v_f, depending on k_b (25), which itself varies with v_{lim}.

Based on the sub-functions f_1 and f_3 of v_f, our method offers several advantages for lane changing compared to other literature approaches: 1) The shape of the sub-functions facilitates smooth velocity changes independent of the behavior of other vehicles. 2) It minimizes overtaking time, crucial for accident prevention with opposing vehicles. 3) The inclusion of subfunction f_3 ensures smooth and comfortable lane changes while maintaining low lateral acceleration during overtaking and lane re-entry. 4) Optimization of subfunction shapes by integrating constraints (26) maintains longitudinal acceleration within defined thresholds without the need for complex optimization algorithms, thus streamlining computation.

2) Road adherence and gradient

Human drivers instinctively tend to decrease vehicle speed in inclement weather conditions, as the braking distance increases with the decrease of the tire grip on the ground. Such precautions are particularly warranted in situations of lower adhesion, as vehicle stability is affected, especially during cornering maneuvers. Hence, it is crucial to account for road adherence (of coefficient μ) in the speed planning approach. The authors of [36] suggested imposing a constraint on acceleration bounds in response to variations in road adherence. In this paper, we propose an adaptation scheme to the percentage of speed reduction as a function of both road adherence and curvature.

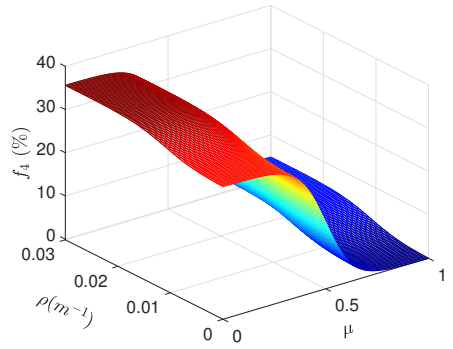

Fig. 7: Sub-function f_4 of v_f in terms of ρ and μ.

Hence, assuming that μ is accessible, define

$$g_1(\mu) = \zeta_1 \frac{1}{1 + e^{-\frac{2\gamma_4}{\overline{\mu}-\underline{\mu}}(|\mu| - \frac{\overline{\mu}+\underline{\mu}}{2})}} + \zeta_2 \tag{28a}$$

$$g_2(\rho_{bf}, \rho_{bp}) = \zeta_3 \frac{1}{1 + e^{-\frac{2\gamma_5}{\overline{\rho}-\underline{\rho}}(|\rho_{bf}|+|\rho_{bp}-\rho_{bf}| - \frac{\overline{\rho}+\underline{\rho}}{2})}} + \zeta_4 \tag{28b}$$

$$f_4(\mu, \rho_{bf}, \rho_{bp}) = g_1(\mu) - g_2(\rho_{bf}, \rho_{bp}) \tag{28c}$$

where ζ_i such that $\{i = 1, 2, 3, 4\}$ are shaping parameters, $\underline{\mu}$ and $\overline{\mu}$ represent the adherence extremities of the transient state of g_1, and γ_4, γ_5 signify the gradient intensity of the transient-state centroid of g_1 and g_2 respectively. The objective is to reduce the speed (increase the speed reduction percentage) with increasing curvature and decreasing adherence. The lateral acceleration a_y, a critical factor influencing vehicle stability, is approximated by (29) [38]. Consequently, to maintain stability, the maximum allowable lateral acceleration diminishes as μ decreases. Conversely, the rate of the side-slip angle $\dot{\beta}$ escalates during cornering, thereby augmenting a_y. Hence, according to (29), reducing v can mitigate a_y to enhance stability as μ decreases and ρ increases.

$$a_y \simeq v(\dot{\psi} + \dot{\beta}) \leq \mu g \tag{29}$$

The reshaping of the function is performed by determining ζ_i according to the desired values of f_4 on the extremities of the transient states $(\underline{\mu}, \overline{\mu}, \underline{\rho}, \overline{\rho})$. Referring to the form in Fig. 7, denote by A($\overline{\mu}$, $\underline{\rho}$), B($\underline{\mu}$, $\underline{\rho}$), C($\underline{\mu}$,$\overline{\rho}$), and D($\overline{\mu}$,$\overline{\rho}$) the four endpoints of transient states of f_4. The value of f_4 at these points is given by (30).

$$f_4|_A = \left[\frac{1}{1+e^{-\gamma_4}}\right]\zeta_1 - \left[\frac{1}{1+e^{\gamma_5}}\right]\zeta_3 + (\zeta_2 - \zeta_4) \tag{30a}$$

$$f_4|_B = \left[\frac{1}{1+e^{\gamma_4}}\right]\zeta_1 - \left[\frac{1}{1+e^{\gamma_5}}\right]\zeta_3 + (\zeta_2 - \zeta_4) \tag{30b}$$

$$f_4|_C = \left[\frac{1}{1+e^{\gamma_4}}\right]\zeta_1 - \left[\frac{1}{1+e^{-\gamma_5}}\right]\zeta_3 + (\zeta_2 - \zeta_4) \tag{30c}$$

$$f_4|_D = \left[\frac{1}{1+e^{-\gamma_4}}\right]\zeta_1 - \left[\frac{1}{1+e^{-\gamma_5}}\right]\zeta_3 + (\zeta_2 - \zeta_4) \tag{30d}$$

Let g_1 and g_2 have the same slope intensity and denote $\gamma* = \gamma_4 = \gamma_5$. Then,

$$\begin{bmatrix} \zeta_1 \\ \zeta_3 \\ \zeta_2 - \zeta_4 \end{bmatrix} = \begin{bmatrix} \frac{1}{1+e^{-\gamma*}} & 1 & \frac{-1}{1+e^{\gamma*}} \\ \frac{1}{1+e^{\gamma*}} & 1 & \frac{-1}{1+e^{\gamma*}} \\ \frac{1}{1+e^{-\gamma*}} & 1 & \frac{-1}{1+e^{-\gamma*}} \end{bmatrix}^{-1} \times \begin{bmatrix} b_1 \\ b_2 \\ b_3 \end{bmatrix} \tag{31}$$

where $\mathscr{B} = [b_1\ \ b_2\ \ b_3]^T$ is the desired values of f_4 at A, B, and C respectively. Fig. 7 depicts the shape of f_4 for $\underline{\mu} =$

0.3, $\overline{\mu} = 0.7$, $\gamma^* = 3$, and $\mathscr{B} = [0.35 \;\; 30 \;\; 35]^T$.

Therefore, v_f is adapted to f_4 by defining v_{f2} as follows

$$v_{f2} = v_{f1}\Big[1 - \frac{f_4}{100}\Big] \tag{32}$$

Another factor influencing the speed reference profile in accordance with human drivers' intuitive responses is road elevation. To the best of the authors' knowledge, no study has yet addressed the incorporation of road slope variations into speed planning methodologies. However, when ascending a steep incline, it is prudent to reduce speed to conserve energy and enhance traction. Conversely, during descent on a steep slope, precise speed management is essential to guarantee safety and stability, as excessive speed may result in loss of control or components overheating. To illustrate the impact of speed control on inclined roads on energy economy, consider the power consumption (P) model (33) [43].

$$P = \Big[ma + (\frac{\rho_a}{2} C_D A_f)v^2 + f_r mg + mg\sin\phi_r\Big]v \tag{33}$$

where m is the vehicle mass, ρ_a is the air density, C_D is the drag coefficient, A_f is the front surface area of the vehicle, f_r is the rolling resistance coefficient, and g is the gravitational constant. Suppose that it is desired to keep the same power of the vehicle for an inclination ϕ_r, i.e. the power required for driving on a straight, non-inclined road equals the power needed for traversing the inclined road. Further, consider that the speed on a zero-degree incline (v_i) is directly proportional to the speed on an inclined road with an angle ϕ_r (v_n), given as $v_n = \lambda v_i$, where $\lambda \in [0, 1]$. Given that aerodynamic forces typically have a less pronounced impact compared to gravitational forces on an incline, and for the sake of simplicity in analysis, the effect of aerodynamic force is neglected. The reduction parameter λ is given as (34).

$$\lambda = \frac{ma + f_r mg}{mg\sin\phi_r + ma + f_r mg} \propto \frac{1}{1 + \frac{g}{|a|}\sin\phi_r} \tag{34}$$

It can be observed in (34) that as the road angle ϕ increases, λ should be decreased to preserve the power consumption. Therefore, neglecting the speed regulation and maintaining a constant velocity on inclined roads could result in increased energy consumption. It's important to highlight that the energy consumption model utilized in our study differs from the one represented by (33), where the detailed energy consumption model is outlined in our previous work [34]. However, for the sake of clarity and comprehensibility, we chose to illustrate the energy economy on inclined roads using the power consumption model (33).

Although road elevation is typically irrelevant to speed profiling for autonomous driving, its rate of change holds significant importance. The road slope or gradient ($grad$) serves as a standard metric for quantifying the angle of road elevation from the ground. It is commonly expressed as a grade percentage and defined as the ratio of rise over run. Considering that the road slope information is typically provided through traffic signs, we assume its availability and awareness by the autonomous vehicle. The consideration of road gradient becomes notably pivotal during cornering as it proportionally affects lateral stability (29). Hence, the objective is to increase the percentage of speed reduction, via a new sub-function, with increasing road gradient and curvature.

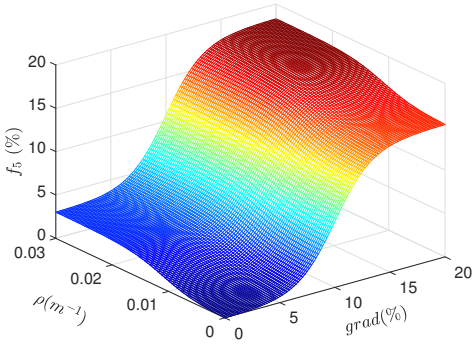

Fig. 8: Sub-function f_5 of v_f in terms of ρ and χ.

Denoting χ as the road gradient, define f_5 as a function of road gradient and curvature as

$$h_1(\mu) = \sigma_1\Big[1 - \frac{1}{1 + e^{-\frac{2\gamma_6}{\overline{\chi} - \underline{\mu}}(|\chi| - \frac{\overline{\chi}+\underline{\chi}}{2})}}\Big] + \sigma_2 \tag{35a}$$

$$h_2(\rho_{bf}, \rho_{bp}) = \sigma_3 \frac{1}{1 + e^{-\frac{2\gamma_7}{\overline{\rho} - \underline{\rho}}(|\rho_{bf}| - \frac{\overline{\rho}+\underline{\rho}}{2})}} + \sigma_4 \tag{35b}$$

$$f_5(\mu, \rho_{bf}, \rho_{bp}) = h_1(\mu) - h_2(\rho_{bf}, \rho_{bp}) \tag{35c}$$

where σ_i are shaping parameters, $\underline{\chi}$ and $\overline{\chi}$ are the road gradient extremities of the transient state of h_1, and γ_6, γ_7 are as γ_5. Following the same reshaping steps as performed in f_4, we have

$$\begin{bmatrix} \sigma_1 \\ \sigma_3 \\ \sigma_2 - \sigma_4 \end{bmatrix} = \begin{bmatrix} \frac{1}{1+e^{-\gamma_2 *}} & 1 & \frac{-1}{1+e^{\gamma_2 *}} \\ \frac{1}{1+e^{\gamma_2 *}} & 1 & \frac{-1}{1+e^{\gamma_2 *}} \\ \frac{1}{1+e^{-\gamma_2 *}} & 1 & \frac{-1}{1+e^{-\gamma_2 *}} \end{bmatrix}^{-1} \times \begin{bmatrix} p_1 \\ p_2 \\ p_3 \end{bmatrix} \tag{36}$$

where $\mathscr{P} = [p_1 \;\; p_2 \;\; p_3]^T$ is the desired values of f_5 at ($\overline{\chi}$, $\underline{\rho}$), ($\underline{\chi}$, $\underline{\rho}$), and ($\underline{\chi}$,$\overline{\rho}$) respectively. By setting $\underline{\chi} = 5$, $\overline{\chi} = 15$, $\gamma_2^* = 3.5$, and $\mathscr{B} = [0.2 \;\; 15 \;\; 18]^T$, the shape of f_5 is depicted in Fig. 8.

$$F_{z,fl} = m\Big[\frac{l_r}{l_r + l_f} g\cos(\phi_r) - \frac{h}{l_r + l_f} g\sin(\phi_r) - \frac{h}{l_r + l_f} a_x\Big] \times \Big[\frac{1}{2} - \frac{h}{t_f g} a_y\Big] \tag{37a}$$

$$F_{z,fr} = m\Big[\frac{l_r}{l_r + l_f} g\cos(\phi_r) - \frac{h}{l_r + l_f} g\sin(\phi_r) - \frac{h}{l_r + l_f} a_x\Big] \times \Big[\frac{1}{2} + \frac{h}{t_f g} a_y\Big] \tag{37b}$$

$$F_{z,rl} = m\Big[\frac{l_f}{l_r + l_f} g\cos(\phi_r) + \frac{h}{l_r + l_f} g\sin(\phi_r) + \frac{h}{l_r + l_f} a_x\Big] \times \Big[\frac{1}{2} - \frac{h}{t_r g} a_y\Big] \tag{37c}$$

$$F_{z,rr} = m\Big[\frac{l_f}{l_r + l_f} g\cos(\phi_r) + \frac{h}{l_r + l_f} g\sin(\phi_r) + \frac{h}{l_r + l_f} a_x\Big] \times \Big[\frac{1}{2} + \frac{h}{t_r g} a_y\Big] \tag{37d}$$

The elevation angle of the road from the ground ϕ_r impacts vehicle dynamics by influencing the tire loads F_z. Denote by

m the vehicle mass, h is the height of the vehicle center of gravity (CG), and l_r and l_f are respectively the distances from CG to the rear and front axles. Then, the tire loads derived from [44], can be determined by (37), where $\{fl, fr, rl, rr\}$ represent the tires: front-left, front-right, rear-left, and rear-right respectively. g is the gravitational acceleration, and t_r and t_f are the rear and front tracks respectively. ϕ_r and χ are related according to (38).

$$\phi_r = \arctan(\chi(\%)/100) \tag{38}$$

Finally, the planning parameter v_f is given by (39).

$$v_f = v_{f2}\Big[1 - \frac{f_5}{100}\Big] \tag{39}$$

As f_5 impacts the tire loads, define the rear/front load distribution ratio κ_1, the left/right load distribution ratio κ_2, and the load transfer ratio LTR [34] to be used as cost variables as follows

$$\kappa_1 = \frac{F_{z,fi}}{F_{z,ri}} = \frac{F_{z,fr} + F_{z,fl}}{F_{z,rr} + F_{z,rl}} \tag{40a}$$

$$\kappa_2 = \frac{F_{z,ir}}{F_{z,il}} = \frac{F_{z,fr} + F_{z,rr}}{F_{z,fl} + F_{z,rl}} \tag{40b}$$

$$LTR = \frac{(F_{z,fr} + F_{z,rr}) - (F_{zrl} + F_{z,fl})}{(F_{z,fr} + F_{z,rr}) + (F_{zrl} + F_{z,fl})} \tag{40c}$$

The physical parameters are bounded as follows: μ is within $\mu \in [0\ 1]$, $|\chi| \in [0\ 20]\,(\%)$, and $|\rho| \in [0\ 0.03]\ m^{-1}$. Functions dependent on μ, χ, or ρ saturate if these parameters exceed their respective ranges.

The formulation of the sub-functions of v_f is developed in a generalized manner. However, the shaping parameters $(\lambda_i, \zeta_i, \sigma_i)$ are tunable and may require adjustment according to the controller characteristics and the desired objectives. For instance, a higher λ_1 decreases the time required for overtaking the succeeding dynamic obstacle. Other parameters depend on the controller characteristics (controllers developed in [34] are depicted in Fig. 1). For instance, lateral controllers with lower path-tracking accuracy may necessitate an increase in λ_2 to reduce the lateral acceleration during cornering and prevent road divergence. Similarly, ζ_2 and $\zeta_2 - \zeta_4$ might require increasing (via b_2 and b_3) to enhance stability in cases of low adherence. The bounds of v_r, ρ, μ, and χ in transient states are heuristic parameters derived from driver experience, multiple simulations, and road data. For instance, $\underline{v_r}$ and $\overline{v_r}$ are chosen to effectively accomplish lane-change within a range of 4 to 7 s. $\underline{\rho}$ and $\overline{\rho}$ are based on real-word road curvature information, while $\underline{\mu}$ and $\overline{\mu}$ and $\underline{\chi}$ and $\overline{\chi}$ are assigned heuristically, with μ constrained within $[0\ 1]$ and χ limited to a maximum of 20 %. This attribute highlights a significant advantage, as the formulation possesses inherent reproducibility, facilitating its straightforward replication and application.

V. Simulation Results

The complete global system architecture is implemented in Simulink/Matlab, tested on a full nonlinear vehicle model [40], and validated on the professional SCANeR Studio vehicle dynamics simulator. The planner is running at a frequency of 10 Hz, the controller is running at 50 Hz, and the rest of the system (vehicle model, bicycle model, energy consumption

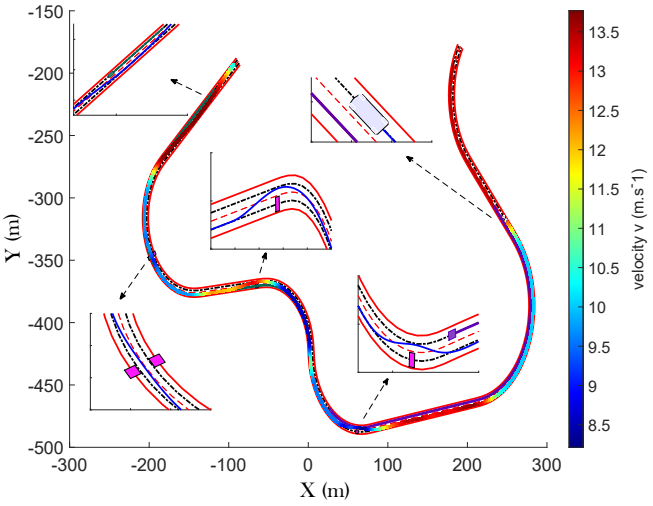

Fig. 9: Vehicle trajectory (same legend as Fig. 2) - sc1.

model) is running at 100 Hz (see the architecture in Fig. 1). At every planning time step, the local occupancy grid is updated to reflect the vehicle's new position, with any mobile obstacles incorporated accordingly.

To illustrate the effectiveness of the proposed speed profiling approach, the following performance variables are introduced.

- Energy consumption $E_m = \int_0^t \sum_{i=1}^{4} \frac{T_i \omega_i}{\eta_{k,i}^{sign(T_i)}}$
- Smoothness costs of:
  - acceleration: $a_{smoothness} = \sum_{i=0}^{n-1} (a_{i+1} - a_i)^2$
  - jerk: $j_{smoothness} = \sum_{i=0}^{n-1} (j_{i+1} - j_i)^2$

This work considers a battery electric vehicle equipped with four independent in-wheel motors. Neglecting the battery internal resistance, the energy consumption E_m is determined as the sum of the energy consumed by the four motors in terms of motor torque T_i, rotational velocity ω_i, and efficiency $\eta_{k,i}$. Further, the efficiency $\eta_{k,i} = \eta_{d,i}$ for driving and $\eta_{k,i} = \eta_{b,i}$ for regenerative braking and they are estimated based on the respective motor efficiency MAPs. For further elaboration, interested readers are directed to the authors' prior work [34].

In order to have a better insight to the contributions, a case study is performed comprising four distinct scenarios. The first three scenario maps represent realistic trajectories extracted from the SCANeR Studio simulator. While the fourth scenario represents a real-world track constructed from a dataset. The first scenario is performed to illustrate the effect of the sub-functions f_1, f_2, and f_3 of v_f and to demonstrate the energy economy of the proposed quintic jerk-controlled speed profiling. The second scenario is carried out to mainly reveal the impact of the sub-function f_4 on vehicle stability in the case of varying load adherence. The third scenario is executed to signify the effectiveness of the sub-function f_5 on steep-slope roads. The final scenario serves to showcase the robustness of our method using real-world datasets while testing it on a full nonlinear vehicle model, demonstrating its viability for on-road application. The proposed quintic speed planning approach is compared with the cubic one and with other literature methods. In particular, the smoothing algorithm methods proposed by [10] and [22] denoted by "SOTA 1". The cubic polynomial approach developed in [14] and labeled

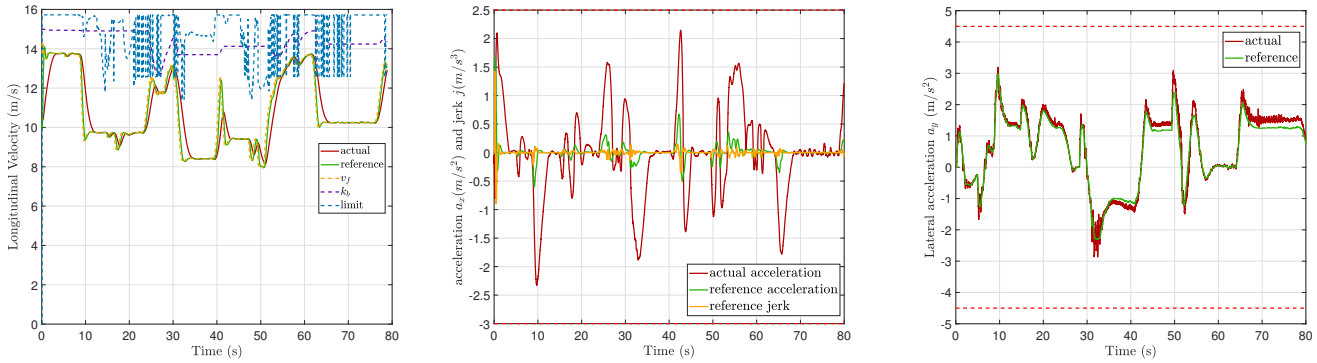

Fig. 10: Quintic speed profile generation, longitudinal acceleration, jerk, and lateral acceleration - sc1.

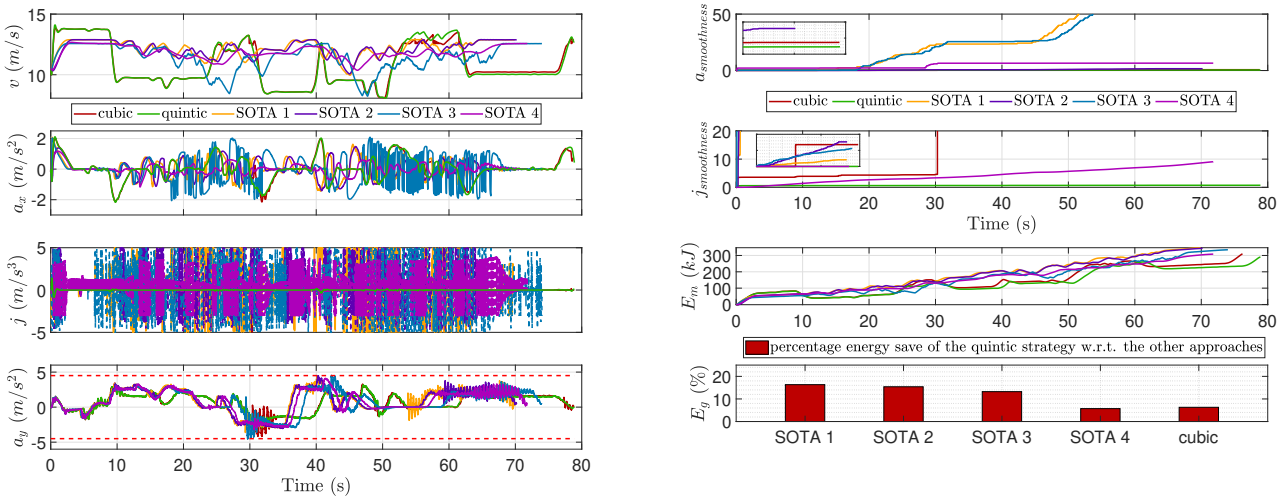

Fig. 11: Comparison of our quintic strategy with literature approaches: acceleration, jerk, smoothness costs, and energy consumption - sc1.

as "SOTA 2". The speed planning approach proposed by [8] considering dynamic safety and denoted by "SOTA 3". Finally, we compare it with the quintic bezier curves generation for speed planning proposed by [45], labeled as "SOTA 4".

A. Scenario 1: Urban Environment Testing - sc1

The initial scenario unfolds on the track depicted in Fig. 9. Within this scenario, the on-road vehicle confronts several typical situations, including: 1) overtaking a moving obstacle, 2) navigating through a narrow passage, 3) executing a lane change maneuver to circumvent a static obstacle at a corner, and 4) re-entering the host lane after encountering a dynamic obstacle while overtaking a static obstacle. Throughout these maneuvers, the curvature of the base frame dynamically varies from low-curvature straight paths to high-curvature corners. The road adherence coefficient is kept at 1 in this scenario and the road gradient is assumed $0\ \%$. The velocity of the vehicle along the tracked path is shown and varies between $8\ m/s$ to $14\ m/s$. Initially, upon deciding to overtake the incoming dynamic obstacle, f_1 (22) is promoted, allowing the vehicle to attain the requisite speed for overtaking in a reasonable time. Subsequently, the vehicle must return to the host lane, and thus f_3 (23b) is activated, aligning with the high curvature of the best path. Subsequently, f_2 (23a) is consistently adapting to the curvature of the base frame, while the lowest speed is achieved when a combination of f_2 and f_3 is ascertained during a lane change maneuver on segments of the high-curvature base frame. The speed profile is depicted in Fig. 10 along with the longitudinal and lateral acceleration and the jerk. The parameter k_b (25) is demonstrated to dynamically adjust according to the speed limitation (13d). Consequently, the planning parameter v_f (39) continually adapts based on variations in k_b, f_1, f_2, and f_3. Utilizing the value of v_f, the reference speed profile is then constructed through quintic polynomial generation. The actual vehicle speed is shown to track the reference-generated profile with smooth acceleration bounded between $-3\ m/s^2$ and $2.5\ m/s^2$. The lateral acceleration is illustrated alongside the reference (which is equal to $\rho.v^2$) constrained within the interval of $[-4\ \ 4]\ m/s^2$. Importantly, it does not exceed $3.5\ m/s^2$, indicative of a notably comfortable and smooth drive.

In the same scenario, under the same test conditions, and based on the constructed profile of v_f, the reference speed profile is generated using a cubic polynomial to contrast it with the quintic polynomial approach. As demonstrated in Fig. 4, the cubic speed profile closely resembles the quintic one, yet exhibits variations in acceleration and jerk profiles. The acceleration and jerk profiles of the quintic and cubic polynomial approaches are given in Fig. 11 along with the energy

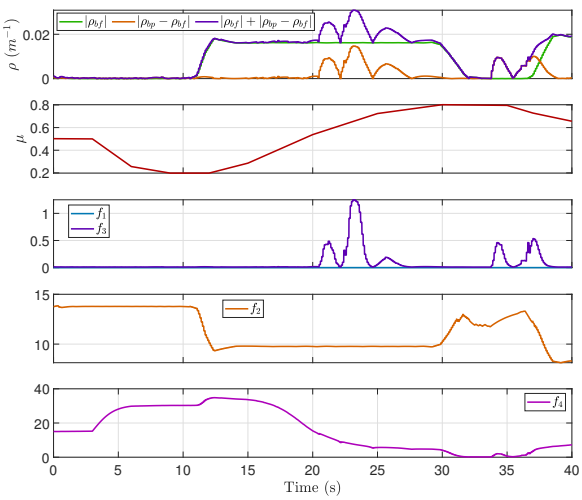

Fig. 12: Profiling the functions of v_f: f_1, f_2, f_3, and f_4 - sc2.

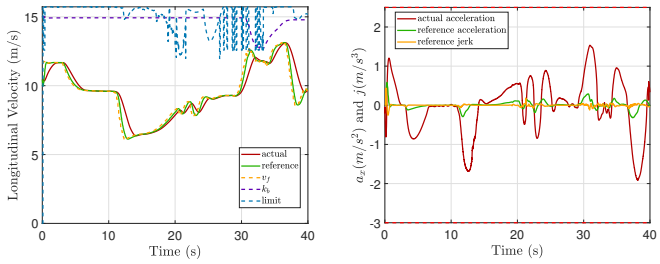

Fig. 13: Speed profiling, acceleration, and jerk - sc2.

consumption and smoothness costs. A noticeable distinction in energy consumption emerges between the two approaches, albeit having the same speed profile. This discrepancy stems from the contrasting smoothness of the jerk profile: the quintic approach features a third-order curve, while the cubic approach exhibits a linear jerk profile. Oscillations and high overshoots in the cubic polynomial's jerk profile are attributable to its unregulated behavior, in contrast to the quintic approach, which imposes constraints on the jerk profile at every planning step (15e,15f) (see Fig. 11). The smoothness costs highlight the superiority of the quintic polynomial approach over the cubic one in terms of acceleration smoothness, with a noteworthy disparity in jerk smoothness. Specifically, the quintic approach achieves a jerk smoothness value below 0.7, while the cubic approach exhibits a value exceeding 100. Consequently, although both approaches yield identical speed profiles, the quintic speed profiling resulted in an energy saving of 6 % compared to the cubic approach, attributed to superior jerk smoothness and control.

Our quintic speed planning is compared further with the literature approaches SOTA 1, SOTA 2, SOTA 3, and SOTA 4. Fig. 11 illustrates their respective reference speed profiles, alongside longitudinal and lateral accelerations, as well as jerk profiles. Although the speed profile of SOTA 1 is smooth, its longitudinal acceleration exhibits oscillations, and its jerk profile is unbounded and oscillatory. SOTA 2 revealed an acceptable behavior in the speed and acceleration profiles but its jerk is oscillatory and unbounded. SOTA 3 exhibited an undesirable behavior in the speed and acceleration profiles

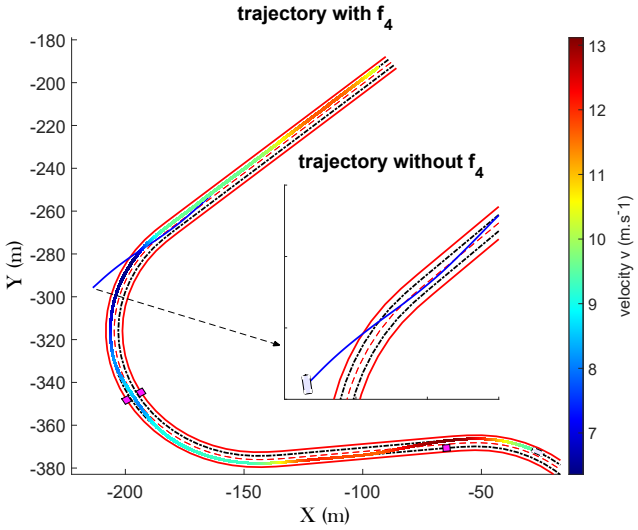

Fig. 14: Vehicle trajectory (same legend as Fig. 2) - sc2.

as well as the jerk profile. In contrast, although SOTA 4 employs quintic bezier curves and implies smooth jerk profiles, it enforces zero jerk at the beginning of the speed profile. Despite being widely adopted in the literature, this constraint renders the jerk profile oscillatory, as it should be zero at each planning iteration, thereby increasing its smoothness costs and energy consumption. The percentage energy save of our quintic strategy compared to SOTA 1, SOTA 2 and SOTA 3 is roughly 15 % and about 6 % compared to SOTA 4. The former reveals the effect of jerk smoothness and control, while the latter underscores the sole impact of jerk control.

B. Scenario 2: Road Adherence Variation - sc2

The second scenario is carried out on the same track featured in the first scenario, encompassing a narrow passage navigation and a lane change maneuver. However, in this scenario, the adherence coefficient μ undergoes continuous variation. The profiling of the v_f sub-functions f_1, f_2, f_3, and f_4 is depicted in Fig. 12 with the curvature variation and adherence changing. It can be observed that f_3 is promoted with the increase of $|\rho_{bp}-\rho_{bf}|$ (see (23b)), and f_2 is adapting in response to $|\rho_{bf}|$. Whereas, f_4 undergoes variation with the decrease of μ and the increase of $|\rho_{bf}|+|\rho_{bp}-\rho_{bf}|$ (28b).

The speed profiling along with the longitudinal acceleration and jerk is shown in Fig. 13. The speed reduction at $t = 10\ s$ is executed in response to f_4 to maintain vehicle stability, particularly on a road with $\mu = 0.2$, indicative of snowy conditions. Despite the significant drop in speed ($\approx 4\ m/s$), the design of v_f and the quintic polynomial prevent the acceleration from reaching $-2\ m/s^2$ and keep its profile smooth. In addition, it conserves the smoothness of jerk and prevents its overshooting despite the road grip conditions.

To gauge the significance of incorporating μ and the efficacy of f_4, a test is conducted without integrating f_4 and subsequently compared with the original test. Fig. 14 illustrates the disparity between the vehicle trajectories with and without the integration of f_4. It is evident that neglecting to address speed modulation in terms of μ, particularly on high-curvature roads, can result in the vehicle losing stability and veering off the

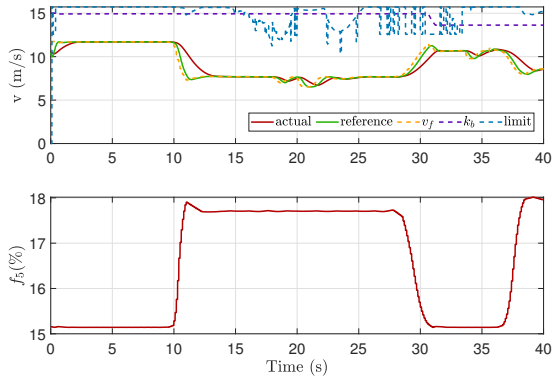

Fig. 15: Quintic speed profiling - sc3.

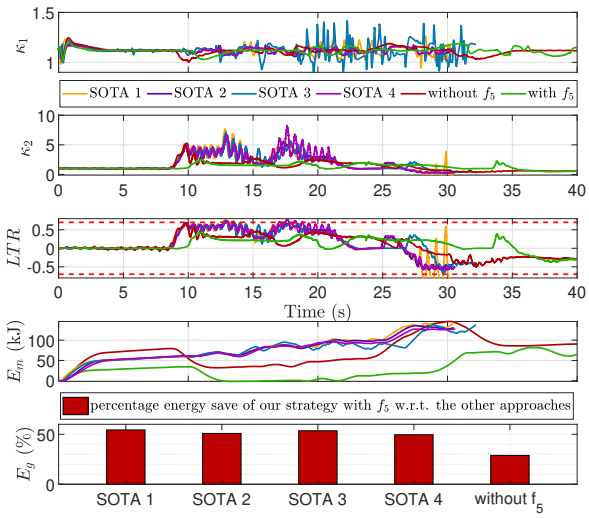

Fig. 16: Cost and performance variables - sc3.

road, potentially leading to severe accidents. The methods in SOTA 1, SOTA 2, SOTA 3, and SOTA 4 exhibited similar behavior, veering off the road. Therefore, it is imperative to incorporate f_4 as a function of road adherence and variation of road curvature in an integrated strategy into speed planning.

C. Scenario 3: Road Gradient Changing - sc3

The third scenario is conducted on the same track as the first scenario, involving navigation through a narrow passage and executing a lane change maneuver. In this scenario, the vehicle operates on a steep slope with a gradient of 15 %. The energy-efficient quintic speed profiling with the variation of v_f in terms of its sub-functions, particularly f_5, is depicted in Fig. 15. Given the consistent road slope throughout the scenario, f_5 varies as a function of the base frame curvature, ensuring it remains above the threshold required for a 15 % gradient.

To assess the importance of integrating χ and the effectiveness of f_5, a test without incorporating f_5 is performed and contrasted with the original one. The literature approaches are also employed and contrasted with our approach. The cost variables (40) are employed for the purpose of comparison and shown in Fig. 16, along with the energy consumption metric. The integration of f_5 is observed to improve load distribution

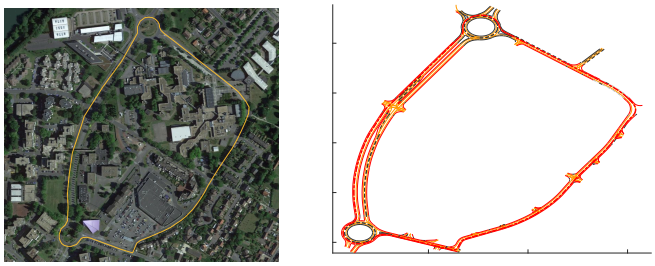

Fig. 17: The real trajectory dataset in the city of Compiègne, France.

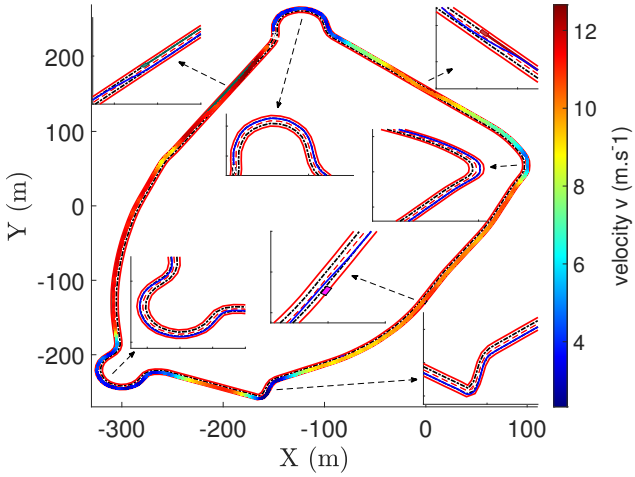

Fig. 18: Vehicle trajectory (same legend as Fig. 2) - sc4.

for both front/rear (κ_1) and right/left (κ_2) orientations. Particularly noteworthy is its role in attenuating oscillations between the right and left loads, which are induced during cornering maneuvers. The load transfer ratio (LTR) is a critical metric for assessing the risk of rollover, with values exceeding the safety threshold of $[-0.75 \;\; 0.75]$ indicating potential danger. The examination revealed that the literature approaches exhibited oscillations in the load transfer and exceeds the bounds of LTR indicating potential danger of rollover. Notably, SOTA 1 surpassed the bounds of $[-1 \;\; 1]$, implying a high risk of rollover. SOTA 3 revealed sharp oscillations in κ_1 which leads to discomfort and higher energy consumption. It is evident that the integration of f_5 has reduced the LTR value to below 0.5, effectively mitigating oscillations and thereby enhancing vehicle stability and comfort. As previously discussed, the precise regulation of speed in the presence of varying road slopes contributes significantly to an energy economy. The energy consumption is given in Fig. 16, illustrating that the integration of f_5 has resulted in energy savings of up to 25 % compared to the scenario without its integration, and up to 50 % compared to the literature approaches.

D. Scenario 4: Validation on a Real-World Dataset - sc4

The final scenario is performed on a track constructed from our real-world dataset. The real track is shown in Fig. 17 and the vehicle trajectory is depicted in Fig. 18. The scenario encompasses a series of maneuvers, commencing with overtaking the succeeding vehicle, followed by navigating

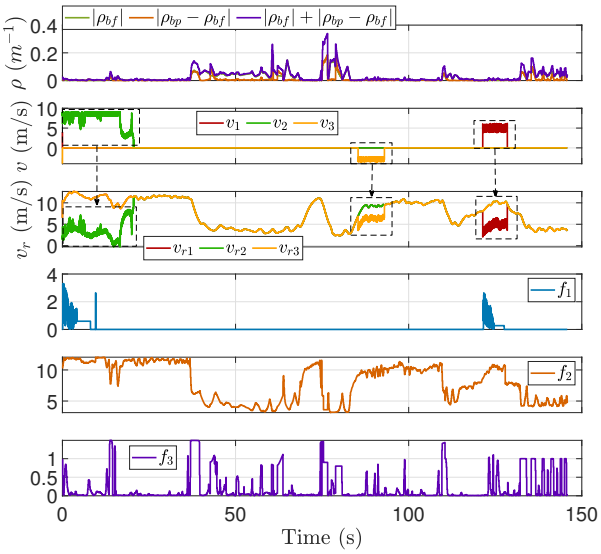

Fig. 19: Profiling of the sub-functions of v_f - sc4.

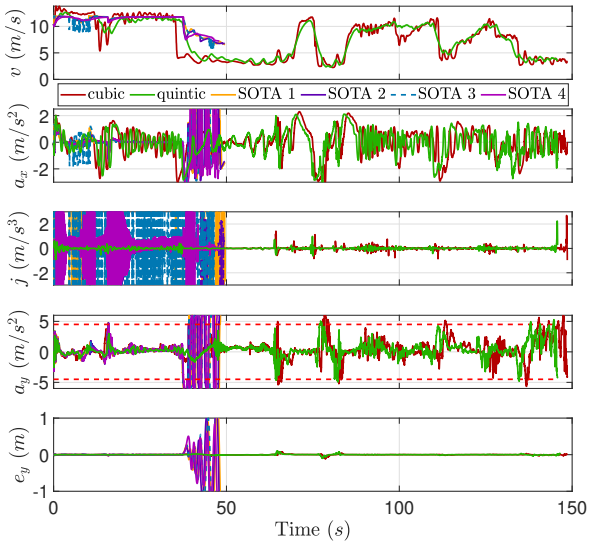

Fig. 20: Comparison between the approaches: vehicle velocity v, longitudinal acceleration a_x, lateral acceleration a_y, and lateral error e_y - sc4.

a roundabout, executing a left turn, and performing a lane change to avoid a stationary vehicle. Subsequently, the ego vehicle overtakes another vehicle before encountering another roundabout. The profiling of the subfunctions of v_f is depicted in Fig. 19. By taking the maximum between ρ_{bf} at the current location and ρ_{bf} at 20 m in front of the vehicle, it becomes feasible to initiate deceleration in anticipation of sharp turns. It should be noted that the dataset track points are sparse and the velocity of other vehicles is noisy. The velocity of other vehicles is available inside the perception zone of the vehicle and assumed zero outside it. The profiling of f_1 is shown in Fig. 19 as a function of the relative velocity $v_{r,i}$. Notably, f_1 is not triggered for $v_{r,3}$, as the moving obstacle 3 is approaching the ego vehicle from the opposite direction on the second lane.

The generated reference velocity profiles of our quintic approach, cubic approach, and the other literature methods are presented in Fig. 20. Due to the nature of the dataset, the use of full nonlinear vehicle model, and the critical situations of the scenario, none of the literature approaches completed the test, despite a maximum velocity setting of 12 m/s. In contrast to the quintic and cubic approaches that follows the parameter v_f, with the quintic having smoother speed profile, jerk, and lower lateral acceleration. As we delve into more realistic real-world scenarios, it becomes crucial for the speed profile to dynamically adjust to road-changing conditions. This underscores the robustness of our approach and its practical applicability for on-road operations.

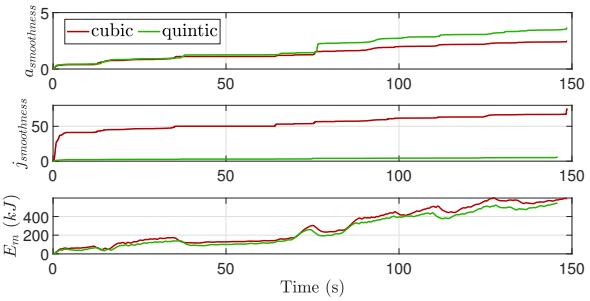

Fig. 21: Smoothness costs and energy consumption comparison - sc4.

The smoothness costs of acceleration and jerk along with the energy consumption for our quintic and cubic approaches are depicted in Fig. 21. Despite the quintic approach exhibiting higher acceleration smoothness, its jerk smoothness is notably lower compared to the cubic approach. Consequently, the energy consumption is lower in the quintic approach, resulting in approximately an 8 % energy savings. This highlights the significant impact of jerk smoothness on energy consumption, outweighing the influence of acceleration smoothness.

E. Recap

The conducted scenarios have revealed the significance of the proposed speed planning strategy. Scenario 1 showcased the effectiveness of the sub-functions f_1, f_2 and f_3 of v_f in handling obstacles and varying road curvature. The quintic speed profiling emphasized energy economy compared to the cubic one, achieved through smooth controlled acceleration and jerk profiles. The proposed approach is subjected to testing in additional scenarios to assess its generality, yielding similar outcomes with slightly varying energy savings values. Scenario 2 elucidated the importance of incorporating road adherence in the speed planning methodologies, and manifested the leading merits of f_4 in handling continuous varying road adherence. Scenario 3 demonstrated the major advantage of integrating road gradient via f_5 in enhancing the overall stability of the vehicle while achieving notable energy savings. Finally, Scenario 4 highlighted the effectiveness and robustness of our approach in real-world situations. In addition to the ablation tests for f_4 and f_5, we conducted individual experiments for f_1, f_2, and f_3. f_1 contributes to efficient overtaking by reducing the time spent on the second lane by 35 %. f_2 is crucial for safety and stability on high curvature roads, and f_3 enhances the lane change comfort by lowering the lateral acceleration.

It is worth noting that the execution time of the speed planning approach with the quintic profiling is roughly similar

to the cubic one. The simulations are conducted under an Intel Core i9-12950HX CPU 2.3-GHz laptop. With a sampling time of $100\ ms$, the quintic speed profiling (including the calculation of k_b and v_f) is executed on average in $0.01\ ms$, while the cubic one in $0.008\ ms$. This demonstrates exceptionally fast execution, coupled with energy efficiency, driving comfort, and enhanced stability. The average total execution time for the entire process is $15\ ms$, making real-time operation feasible.

Videos of the system validation on the Scaner Studio simulator can be seen at: "https://www.youtube.com/playlist?list=PL6pn13pjrt-AomyhzJXOsg-5R6Chb11Ne".

VI. Conclusion

This paper introduces a novel rapid energy-efficient jerk-controlled speed planning methodology based on quintic polynomial generation. Several factors, including relative velocity with obstacles, the curvature of the base frame and best path, road adherence, and road gradient are integrated into a speed planning parameter. The approach is demonstrated to be energy-efficient attributed to the smoothness and control of the jerk profile, and effectively addresses a wide array of critical scenarios within moderate traffic conditions. Future research endeavors may focus on further refining the proposed method to accommodate dense traffic environments.

References

[1] V. Lefkopoulos and M. Kamgarpour, "Trajectory planning under environmental uncertainty with finite-sample safety guarantees," *Automatica*, vol. 131, p. 109754, 2021.

[2] L. Qian, X. Xu, Y. Zeng, X. Li, Z. Sun, and H. Song, "Synchronous maneuver searching and trajectory planning for autonomous vehicles in dynamic traffic environments," *IEEE Intelligent Transportation Systems Magazine*, vol. 14, no. 1, pp. 57–73, 2022.

[3] X. Chen, M. Zhu, K. Chen, P. Wang, H. Lu, H. Zhong, X. Han, X. Wang, and Y. Wang, "Follownet: A comprehensive benchmark for car-following behavior modeling," *Scientific Data*, vol. 10, 11 2023.

[4] Y. Zhang, H. Chen, S. L. Waslander, J. Gong, G. Xiong, T. Yang, and K. Liu, "Hybrid trajectory planning for autonomous driving in highly constrained environments," *IEEE Access*, vol. 6, pp. 32 800–32 819, 2018.

[5] J. Cheng, Y. Chen, Q. Zhang, L. Gan, C. Liu, and M. Liu, "Real-time trajectory planning for autonomous driving with gaussian process and incremental refinement," in *2022 International Conference on Robotics and Automation (ICRA)*, 2022, pp. 8999–9005.

[6] J. Kim, K. Jo, W. Lim, and M. Sunwoo, "A probabilistic optimization approach for motion planning of autonomous vehicles," *Proceedings of the Institution of Mechanical Engineers, Part D: Journal of Automobile Engineering*, vol. 232, no. 5, pp. 632–650, 2018.

[7] R. Mashayekhi, M. Y. I. Idris, M. H. Anisi, I. Ahmedy, and I. Ali, "Informed rrt*-connect: An asymptotically optimal single-query path planning method," *IEEE Access*, vol. 8, pp. 19 842–19 852, 2020.

[8] X. Hu, L. Chen, B. Tang, D. Cao, and H. He, "Dynamic path planning for autonomous driving on various roads with avoidance of static and moving obstacles," *Mechanical Systems and Signal Processing*, vol. 100, pp. 482–500, 2018.

[9] K. Chu, M. Lee, and M. Sunwoo, "Local path planning for off-road autonomous driving with avoidance of static obstacles," *IEEE Transactions on Intelligent Transportation Systems*, vol. 13, no. 4, pp. 1599–1616, 2012.

[10] A. Said, R. Talj, C. Francis, and H. Shraim, "Local trajectory planning for autonomous vehicle with static and dynamic obstacles avoidance," in *2021 IEEE International Intelligent Transportation Systems Conference (ITSC)*, 2021, pp. 410–416.

[11] M. Werling, J. Ziegler, S. Kammel, and S. Thrun, "Optimal trajectory generation for dynamic street scenarios in a frenét frame," in *2010 IEEE International Conference on Robotics and Automation*, 2010, pp. 987–993.

[12] Y. Guo, D. Yao, B. Li, Z. He, H. Gao, and L. Li, "Trajectory planning for an autonomous vehicle in spatially constrained environments," *IEEE Transactions on Intelligent Transportation Systems*, vol. 23, no. 10, pp. 18 326–18 336, 2022.

[13] K. Bergman, O. Ljungqvist, and D. Axehill, "Improved path planning by tightly combining lattice-based path planning and optimal control," *IEEE Transactions on Intelligent Vehicles*, vol. 6, no. 1, pp. 57–66, 2021.

[14] X. Li, Z. Sun, D. Cao, Z. He, and Q. Zhu, "Real-time trajectory planning for autonomous urban driving: Framework, algorithms, and verifications," *IEEE/ASME Transactions on Mechatronics*, vol. 21, no. 2, pp. 740–753, 2016.

[15] W. Lim, S. Lee, M. Sunwoo, and K. Jo, "Hybrid trajectory planning for autonomous driving in on-road dynamic scenarios," *IEEE Transactions on Intelligent Transportation Systems*, vol. 22, no. 1, pp. 341–355, 2021.

[16] M. Wang, L. Zhang, Z. Zhang, and Z. Wang, "A hybrid trajectory planning strategy for intelligent vehicles in on-road dynamic scenarios," *IEEE Transactions on Vehicular Technology*, vol. 72, no. 3, pp. 2832–2847, 2023.

[17] W. Lim, S. Lee, M. Sunwoo, and K. Jo, "Hierarchical trajectory planning of an autonomous car based on the integration of a sampling and an optimization method," *IEEE Transactions on Intelligent Transportation Systems*, vol. 19, no. 2, pp. 613–626, 2018.

[18] T. Lipp and S. Boyd, "Minimum-time speed optimisation over a fixed path," *International Journal of Control*, vol. 87, no. 6, pp. 1297–1311, 2014.

[19] J. Johnson and K. Hauser, "Optimal acceleration-bounded trajectory planning in dynamic environments along a specified path," in *2012 IEEE International Conference on Robotics and Automation*, 2012, pp. 2035–2041.

[20] W. Xu and J. M. Dolan, "Speed planning in dynamic environments over a fixed path for autonomous vehicles," in *2022 International Conference on Robotics and Automation (ICRA)*, 2022, pp. 3321–3327.

[21] E. Ozatay, U. Ozguner, and D. Filev, "Velocity profile optimization of on road vehicles: Pontryagin's maximum principle based approach," *Control Engineering Practice*, vol. 61, pp. 244–254, 2017.

[22] T. Duhautbout, R. Talj, V. Cherfaoui, F. Aioun, and F. Guillemard, "Efficient speed planning in the path-time space for urban autonomous driving," in *2022 IEEE 25th International Conference on Intelligent Transportation Systems (ITSC)*, 2022, pp. 1268–1274.

[23] Y. Zhang, H. Chen, S. L. Waslander, T. Yang, S. Zhang, G. Xiong, and K. Liu, "Speed planning for autonomous driving via convex optimization," in *2018 21st International Conference on Intelligent Transportation Systems (ITSC)*, 2018, pp. 1089–1094.

[24] C. Liu, W. Zhan, and M. Tomizuka, "Speed profile planning in dynamic environments via temporal optimization," in *2017 IEEE Intelligent Vehicles Symposium (IV)*, 2017, pp. 154–159.

[25] Q.-C. Pham, "A general, fast, and robust implementation of the time-optimal path parameterization algorithm," *IEEE Transactions on Robotics*, vol. 30, no. 6, pp. 1533–1540, 2014.

[26] B. Liu, C. Sun, B. Wang, and F. Sun, "Adaptive speed planning of connected and automated vehicles using multi-light trained deep reinforcement learning," *IEEE Transactions on Vehicular Technology*, vol. 71, no. 4, pp. 3533–3546, 2022.

[27] H. Lee, K. Kim, N. Kim, and S. W. Cha, "Energy efficient speed planning of electric vehicles for car-following scenario using model-based reinforcement learning," *Applied Energy*, vol. 313, p. 118460, 2022.

[28] H. Zhang, Y. Zhang, C. Liu, and Z. Zhang, "Energy efficient path planning for autonomous ground vehicles with ackermann steering," *Robotics and Autonomous Systems*, vol. 162, p. 104366, 2023.

[29] E. Joa, H. Lee, E. Y. Choi, and F. Borrelli, "Energy-efficient lane changes planning and control for connected autonomous vehicles on urban roads," in *2023 IEEE Intelligent Vehicles Symposium (IV)*, 2023, pp. 1–6.

[30] W. Dib, A. Chasse, P. Moulin, A. Sciarretta, and G. Corde, "Optimal energy management for an electric vehicle in eco-driving applications," *Control Engineering Practice*, vol. 29, pp. 299–307, 2014.

[31] H. Xu, N. Zhang, Z. Li, Z. Zhuo, Y. Zhang, Y. Zhang, and H. Ding, "Energy-saving speed planning for electric vehicles based on rhrl in car following scenarios," *Sustainability*, vol. 15, no. 22, 2023.

[32] S. Bae, Y. Choi, Y. Kim, J. Guanetti, F. Borrelli, and S. Moura, "Real-time ecological velocity planning for plug-in hybrid vehicles with partial communication to traffic lights," in *2019 IEEE 58th Conference on Decision and Control (CDC)*, 2019, pp. 1279–1285.

[33] A. Desreveaux, A. Bouscayrol, R. Trigui, E. Castex, and J. Klein, "Impact of the velocity profile on energy consumption of electric

vehicles," *IEEE Transactions on Vehicular Technology*, vol. 68, no. 12, pp. 11 420–11 426, 2019.
[34] F. Tarhini, R. Talj, and M. Doumiati, "Dual-level control architectures for over-actuated autonomous vehicle's stability, path-tracking, and energy economy," *IEEE Transactions on Intelligent Vehicles*, vol. 9, no. 1, pp. 287–303, 2024.
[35] A. Artuñedo, J. Villagra, and J. Godoy, "Jerk-limited time-optimal speed planning for arbitrary paths," *IEEE Transactions on Intelligent Transportation Systems*, vol. 23, no. 7, pp. 8194–8208, 2022.
[36] J. Hu, Y. Zhang, and S. Rakheja, "Adaptive lane change trajectory planning scheme for autonomous vehicles under various road frictions and vehicle speeds," *IEEE Transactions on Intelligent Vehicles*, vol. 8, no. 2, pp. 1252–1265, 2023.
[37] Y. Shimizu, T. Horibe, F. Watanabe, and S. Kato, "Jerk constrained velocity planning for an autonomous vehicle: Linear programming approach," in *2022 International Conference on Robotics and Automation (ICRA)*, 2022, pp. 5814–5820.
[38] F. Tarhini, R. Talj, and M. Doumiati, "Dynamic and real-time continuous look-ahead distance for autonomous vehicles: an explicit formulation," *Vehicle System Dynamics*, 2023.
[39] ——, "Multi-objective control architecture for an autonomous in-wheel driven electric vehicle," *IFAC-PapersOnLine*, vol. 56, no. 2, pp. 11 470–11 476, 2023.
[40] A. Chokor, R. Talj, A. Charara, H. Shraim, and C. Francis, "Active suspension control to improve passengers comfort and vehicle's stability," in *2016 IEEE 19th International Conference on Intelligent Transportation Systems (ITSC)*, 2016, pp. 296–301.
[41] *SCANeR - AVSimulation*, SCANeR Studio Simulator. [Online]. Available: https://www.avsimulation.com/scaner/
[42] T. Barfoot and C. Clark, "Motion planning for formations of mobile robots," *Robotics and Autonomous Systems*, vol. 46, no. 2, pp. 65–78, 2004.
[43] A. Sciarretta, G. De Nunzio, and L. L. Ojeda, "Optimal ecodriving control: Energy-efficient driving of road vehicles as an optimal control problem," *IEEE Control Systems Magazine*, vol. 35, no. 5, pp. 71–90, 2015.
[44] R. Jazar, *Vehicle dynamics: Theory and application, second edition*, 01 2014.
[45] D. González, V. Milanés, J. Pérez, and F. Nashashibi, "Speed profile generation based on quintic bézier curves for enhanced passenger comfort," in *2016 IEEE 19th International Conference on Intelligent Transportation Systems (ITSC)*, 2016, pp. 814–819.